Progress in Photovoltaics: Research and Applications

WILEY

PROGRESS IN PHOTOVOLTAICS

RESEARCH ARTICLE OPEN ACCESS

Sodium Induced Beneficial Effects in Wide Bandgap Cu(In,Ga)S_2 Solar Cell With 15.7% Efficiency

Arivazhagan Valluvar Oli[1] | Kulwinder Kaur[1] | Michele Melchiorre[1] | Aubin Jean-Claude Mireille Prot[1] | Sevan Gharabeiki[1] | Yucheng Hu[2] | Gunnar Kusch[2] | Adam Hultqvist[3] | Tobias Törndahl[3] | Wolfram Hempel[4] | Wolfram Witte[4] | Rachel A. Oliver[2] | Susanne Siebentritt[1]

[1]Laboratory for Photovoltaics, Department of Physics and Materials Science Research Unit, University of Luxembourg, Belvaux, Luxembourg | [2]Department of Materials Science and Metallurgy, University of Cambridge, Cambridge, UK | [3]Ångström Solar Center, Division of Solar Cell Technology, Department of Materials Science and Engineering, Uppsala University, Uppsala, Sweden | [4]Zentrum für Sonnenenergie- und Wasserstoff-Forschung Baden-Württemberg (ZSW), Stuttgart, Germany

Correspondence: Arivazhagan Valluvar Oli (arivazhagan.valluvaroli@gmail.com) | Susanne Siebentritt (susanne.siebentritt@uni.lu)

Received: 15 March 2025 | **Revised:** 30 July 2025 | **Accepted:** 11 November 2025

ABSTRACT

This study underscores the pivotal role of sodium (Na) supply in optimizing the optoelectronic properties of wide bandgap (~1.6 eV) Cu(In,Ga)S_2 (CIGS) thin-film absorbers for high-efficiency solar cells. Our findings demonstrate that the synergistic use of Na from the glass substrate, in conjunction with in situ sodium fluoride (NaF) co-evaporation, significantly enhances the structural and optoelectronic properties of the CIGS. CIGS grown under either Na-deficient or excess conditions exhibit inferior microstructural and optoelectronic properties, whereas an optimal Na supply leads to enhanced photovoltaic performance. Optimal Na incorporation minimizes vertical gallium fluctuations and improves the grain size and crystallinity. An absolute 1 sun calibrated photoluminescence (PL) measurement reveals a substantial suppression of bulk defects and a reduction in non-radiative losses, resulting in a high quasi-Fermi level splitting (ΔE_F) of 1.07 eV, 93 meV higher than in Na-deficient CIGS with the same bandgap. Optimal Na supply further increases excited carrier decay time, as revealed from time-resolved PL, and hole doping density. Cross-sectional hyperspectral cathodoluminescence mapping reveals that optimal Na supply significantly reduces defect density near the surface, thereby effectively translating ΔE_F to open-circuit voltage (V_{OC}). As a result, a champion wide bandgap CIGS solar cell with a cadmium-free $ZnSnO_x$ buffer layer achieved an impressive V_{OC} of 971 meV and an active area power conversion efficiency of 15.7%, highlighting its potential for advancing tandem photovoltaic technologies with a stable inorganic top cell.

1 | Introduction

Sulfide-based chalcopyrite with the composition Cu(In,Ga)S_2 (CIGS) is particularly promising as a top cell in tandem solar cell configurations due to its tunable direct bandgap (E_g), ranging from 1.55 eV ($CuInS_2$) to 2.4 eV ($CuGaS_2$) [1]. Chalcopyrite solar modules have demonstrated long-term environmental stability in field tests [2, 3], making them a viable candidate for commercialization. Additionally, the growth techniques used for CIGS, such as physical vapor deposition, can be seamlessly integrated into existing large-scale manufacturing processes employed for low-bandgap solar cells based on materials like Cu(In,Ga)Se_2 (CIGSe) [4, 5]. Despite the progress in increasing the power conversion efficiency (PCE) of CIGS to over 15% [6–8], it still lags behind its selenium (Se) counterpart, which has recently achieved a certified PCE of 23.6% [9]. The primary factor limiting the performance of CIGS solar cells is the open-circuit voltage (V_{OC}) deficit [10, 11]. The V_{OC} is closely related to the quasi-Fermi level splitting (ΔE_F) of the photovoltaic absorber, which represents the maximum V_{OC} that a solar cell can achieve with ideal interfaces [12, 13]. Non-radiative recombination channels, which arise from defects within the

absorber and at the interfaces, contribute to a ΔE_F deficit (referred to as "non-radiative loss" throughout the text) defined as the difference between the ideal Shockley–Queisser (SQ) V_{OC} and ΔE_F [7, 14, 15]. This non-radiative loss reduces the minority carrier lifetime and thus V_{OC} in Cu(In,Ga)S_2 solar cells [7, 16, 17]. Therefore, understanding and mitigating these defects is crucial for obtaining high-quality absorbers [12, 13]. Interface recombination is another important factor, which limits the V_{OC} due to band misalignment and interface defects [18, 19]. Strategies such as substrate temperature control, composition engineering, and doping have been widely employed to achieve high-quality sulfide solar cell absorbers [6, 7, 20–22]. CIGS grown at high deposition temperatures and with copper (Cu)-poor stoichiometry has achieved the highest reported PCE of over 15% [6–8]. High deposition temperature increases the grain size due to improved elemental diffusion, while Cu-poor surface compositions help suppress the deep defects and improve the solar cell performance [7, 20].

Sodium (Na) has been known to play a vital role in the improved performance of selenide-based chalcopyrite solar cells through various mechanisms [23–27]. In CIGSe, Na is typically introduced through diffusion from soda-lime glass (SLG) substrates, precursor layers, post-deposition treatments (PDT), or co-evaporation during growth [24, 26, 28, 29]. The presence of Na improves CIGSe absorber performance by mechanisms including substitution of antisite donor defects (e.g., Na_{In} or Na_{Cu}), formation of Cu vacancy (V_{Cu}), passivation of grain boundaries, enhanced atomic diffusion, increased p-type conductivity, and grain size enlargement [30–34]. However, excessive Na content in the absorber can be detrimental to solar cell performance [35–37]. The method of Na incorporation also significantly influences its effect. For example, a statistical comparison in CIGSe found that NaF PDT yielded better absorber quality and solar cell performance compared with the same amount of NaF co-evaporated during growth [27]; however, to our knowledge, no similar comparative study has so far been published that addresses the impact of Na in CIGS. A theoretical study on Na's effect within CIGSe grains proposes that Na supplied via SLG or PDT forms Na_{Cu} antisites during high-temperature growth, which then diffuse to grain boundaries (GB) upon cooling, creating Cu vacancies that increase p-type conductivity [32]. Observation of indium (In) and gallium (Ga) inter grain diffusion promoted by Na revealed that Na segregation at CIGSe GB plays a decisive role by acting as a barrier for In/Ga inter grain diffusion in CIGSe absorber [33]. Given the similarities between sulfide and selenide chalcopyrites, the effects of Na in CIGSe provide valuable insights for understanding its role in CIGS [10]. Similar to CIGSe, Na diffusion from SLG during CIGS growth has been found to enhance hole doping density and yield higher PCE than low-Na absorbers [38]. Additionally, Cu-poor CIGS absorbers grown with optimal NaF precursor layers exhibited improved V_{OC}, which decreased with further increases in NaF thickness [22]. Preliminary investigations suggest that Na diffusion from SLG and NaF co-evaporation during CIGS growth positively affect ΔE_F, while the precursor layer approach had a negative impact [10]. Despite these insights, the specific effects and optimal methods of Na incorporation in CIGS remain underexplored, highlighting the need for further comparative studies in this area.

Here, we study the impact of Na addition on the optoelectronic and structural properties of CIGS, particularly its influence on defects, recombination dynamics, non-radiative losses, ΔE_F, and grain size. Specifically, radiative recombination and defect concentration across the depth of graded bandgap CIGS absorbers have not yet been investigated. This study addresses these gaps by systematically introducing Na into the absorber and examining its effects from optoelectronic, microstructural, and solar cell perspectives. We investigated three different methods to control the Na supply: using a low Na containing glass (LNG) substrate, using an SLG substrate, and adding extra Na via NaF co-evaporation during the second stage of CIGS growth on SLG. We explored Na's impact on the graded bandgap absorber through elemental depth profiling and correlated these findings with microstructural and optoelectronic characterizations. We employed absolute calibrated photoluminescence (PL) measurements, time-resolved PL, and cathodoluminescence (CL) spectroscopy to study optoelectronic transitions and address various defects and non-radiative losses. Furthermore, hyperspectral CL cross-sectional mapping was extensively used to understand recombination paths across the absorber depth and investigate the defect concentration near the space-charge region (SCR). Our results demonstrate that unintentional Na supply from the substrate during CIGS growth is crucial for reducing deep defects. However, introducing Na intentionally and in a controlled manner through co-evaporation during growth provides additional benefits by reducing bulk defects, minimizing non-radiative losses, and increasing grain size and hole doping density. Furthermore, by identifying and mitigating defect density near the surface, we enhance the translation of the absorber's ΔE_F into higher V_{OC} in the final solar cell, with reduced interface losses. Finally, we report that a champion solar cell fabricated with a cadmium-free buffer layer achieved a V_{OC} of 971 meV and an active area PCE of 15.7%. This work paves the way to mitigating the V_{OC} deficit, a key challenge in CIGS, and positions CIGS as a promising wide bandgap absorber for the development of high efficiency tandem photovoltaics.

2 | Results and Discussion

The CIGS absorbers were deposited using a three-stage evaporation process (refer to the deposition profile in Figure S1). To explore the effects of different Na supplies, we utilized two distinct substrates: LNG with low Na content and SLG with relatively high Na content. Na from these substrates diffuses out at high temperatures, serving as a source during CIGS growth [24]. To introduce additional Na, further samples were prepared by co-evaporating NaF during the second stage of CIGS growth on SLG, with source temperatures varying from 600°C to 750°C in 50°C intervals [39]. Increasing the NaF source temperature, while keeping the evaporation time constant, results in a higher Na supply in the absorber during growth. Above an NaF source temperature of 750°C, the absorbers began to peel off upon removal from the vacuum chamber, an issue also reported in CIGSe absorbers prepared via the precursor method when exposed to excess NaF [40]. We assessed the quality of all the absorbers using absolute PL measurements (Figure S7 and Table S1) and found that the 650°C NaF condition resulted in minimized non-radiative recombination losses, supporting its identification as the optimal Na supply. For simplicity and to

facilitate better comparisons, we present the results as LNG (Na-poor), SLG (standard Na), 650 NaF (optimal Na), and 750 NaF (excess Na) throughout the main text. Some results for 600°C and 700°C NaF are included in the supporting information and will be referred to in the main text as appropriate.

Energy-dispersive X-ray spectroscopy (EDS) was conducted at 20 kV to estimate the bulk composition of the absorbers. Figure 1a presents the bulk composition in terms of [Cu]/([Ga] + [In]) (CGI) and [Ga]/([Ga] + [In]) (GGI) ratios. The surface CGI and GGI ratios were measured at 7 kV to capture the signal from the topmost absorber layer and are shown in Figure S2. No significant differences between near surface and bulk composition are found. The compositions of all absorbers are within a similar range, except for LNG, which exhibits a slightly higher CGI. A CGI <1 indicates a Cu-poor stoichiometry, necessary for optimal solar cell operation [7, 22]. Glow discharge optical emission spectroscopy (GDOES) was employed to trace the elemental depth profile of the absorbers. The absorber depth was estimated using the onset Mo signal from GDOES (Figure S3) and correlated with thickness measurements obtained from cross-sectional SEM images (Figure 2). Figure 1b displays the vertical Na concentration profiles (in ppm) of the absorbers. LNG exhibits negligible Na concentration, while SLG shows a high concentration, confirming that Na diffused from the substrate. This observation is consistent with previous studies on CIGSe absorbers grown on alkali-free and SLG substrates, where Na presence was traced through binding energy or depth profiling [25, 27, 28, 40]. The 650 NaF absorber shows slightly lower Na levels than SLG, whereas the 750 NaF absorber exhibits higher Na concentration throughout the absorber depth. We later discuss a possible explanation for the lower Na concentration in the 650 NaF absorber, relating it to increased grain size and lower density of grain boundaries.

Figure 1c,d show the GGI and CGI depth profiles of the absorbers, respectively. The high signal at the surface (indicated by the grey box) is associated with artifacts, complicating the determination of GGI and CGI variations near the surface. The LNG absorber shows a broad notch, a minimum GGI point which represents E_g in a graded absorber, located around 0.5 μm from the surface, while the SLG absorber displays a sharp notch close to the surface, with steep grading toward the back contact. This grading toward the back contact is intentional in three-stage-grown chalcopyrite absorbers, since conduction band edge grading can prevent photogenerated electrons from reaching the back contact [41]. The magnitude of this grading primarily depends on factors such as gallium flux over time, substrate temperature, and dopants like Na or silver as reported for selenide chalcopyrite absorbers [33, 36, 42]. Adding 650 NaF does not affect the notch position but does shift the GGI minimum upward and reduces the vertical GGI grading. The GGI grading gradually increases from the notch through more than half of the absorber depth, then flattening slightly toward the back contact. However, with 750 NaF, the notch widens, shifts downward, and the GGI grading becomes steeper toward the back contact. This

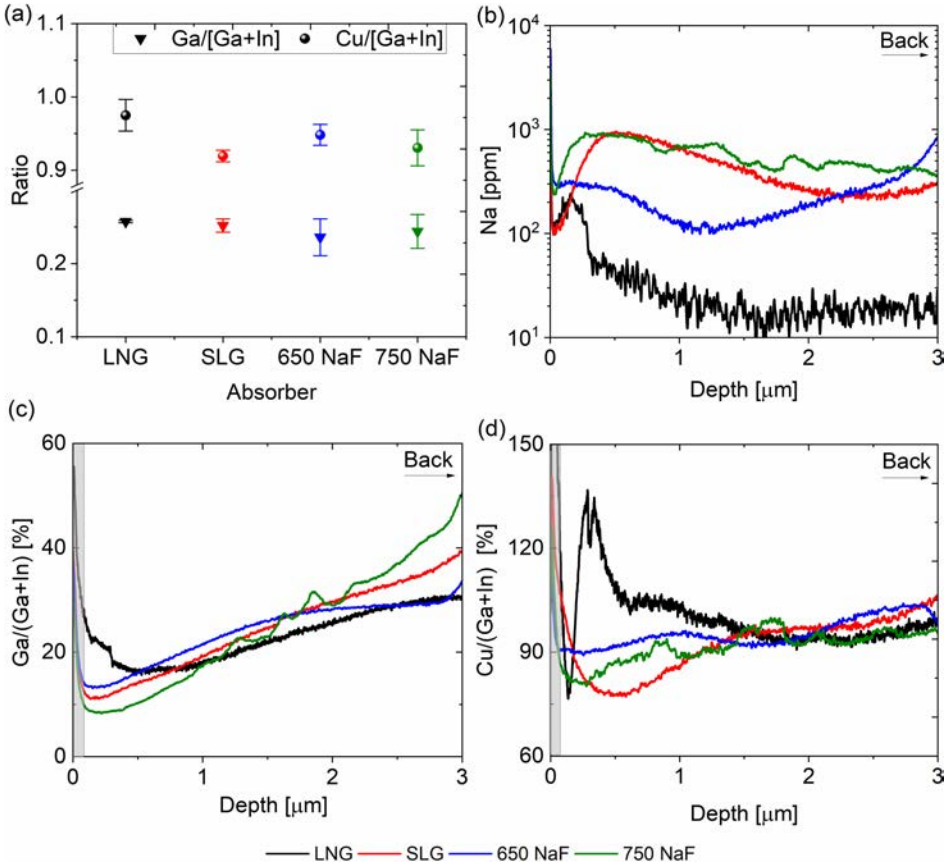

FIGURE 1 | Elemental composition of CIGS with varying Na supply during growth. (a) Bulk [Ga]/([Ga + In]) and [Cu]/([Ga + In]) ratios obtained from EDS. GDOES depth profile of (b) Na concentration, (c) GGI ratio, and (d) CGI ratio. The data points in the near surface region highlighted with a grey rectangle in (c) and (d) are mainly due to artifacts.

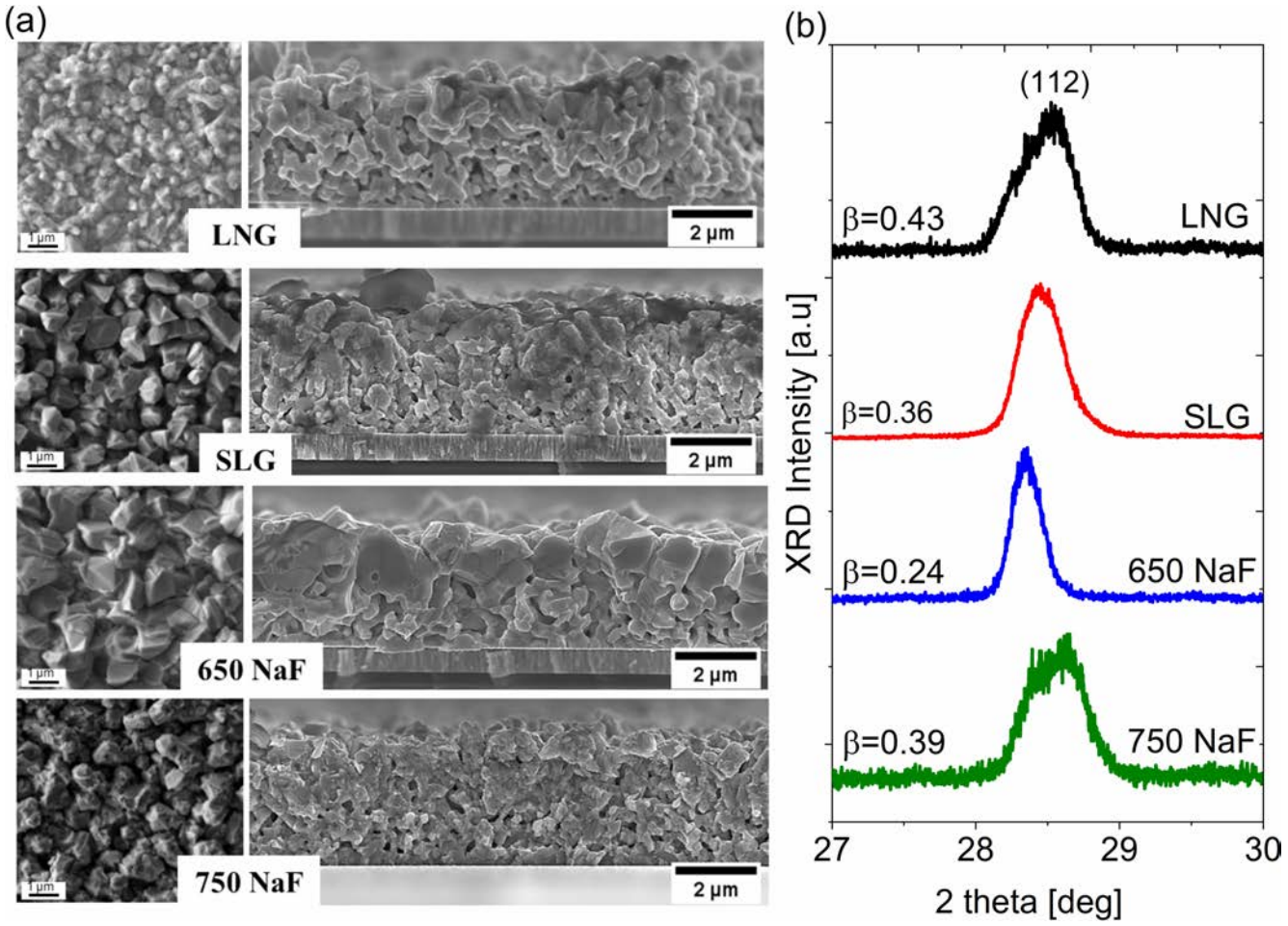

FIGURE 2 | Microstructure of CIGS with different Na supplied during growth. (a) SE images showing top (left) and cross-sectional (right) views. The scale bar in top view images is 1 µm. (b) X-ray diffractograms of the 112 reflex with corresponding full-width half maximum (β) values.

result is consistent with literature comparing Na-free and Na-containing CIGSe absorbers, where variations in Ga concentration were evident in the absorber depth for samples with high Na content [29, 33, 43]. One possible reason for the Na-modulated GGI depth profile variation is improved intragrain diffusion of Ga/In, as Na impedes Ga/In intergrain diffusion by segregating at grain boundaries [33]. We speculate that an abrupt increase in CGI near the surface of the LNG absorber in Figure 1d leads to CuS_x segregation due to insufficient Ga/In intragrain diffusion, resulting from limited Na supply during growth. Figure S3 presents the S, Cu, In, and Ga elemental depth profiles for all absorbers. It is evident that all the absorbers are In-rich near the front surface, except for LNG, and Ga-rich near the Mo back contact, in agreement with the three-stage deposition profile. Sulfur (S) and Cu are almost uniformly distributed across the depth relative to Ga and In. The fluctuations observed in the 750 NaF absorbers is due instability of plasma during the measurement. For double-graded absorbers, an increase in GGI near the surface, as seen in LNG, is preferred. However, all other absorbers exhibit low GGI grading with a less pronounced notch, which would require nearly perfect passivation of the interface with the buffer layer for optimized solar cell operation.

Figure 2a displays top view (left) and cross-sectional (right) scanning electron microscopy (SEM) images of CIGS absorbers with different Na supplies. The absorber grown on LNG exhibits smaller surface grains, whereas the grain size increases with the use of SLG substrate, consistent with literature based on selenides [24]. However, in the cross-section, the SLG appears to have grain structures similar to those of the LNG, which may be attributed to inhomogeneities within the SLG absorber. The addition of NaF at a temperature of 650°C enlarges the grain size, so that grains almost extend from top to bottom in a columnar structure as observed in the cross-sectional images. Conversely, 750 NaF reduces the grain size, leading to smaller grains and exhibiting a rough morphology (see enlarged SE image in Figure S4). Cross-sectional SEM images for 600 and 700 NaF are shown in Figure S4, which resemble the SLG and 750 NaF morphological features, respectively. Generally, moderate Na supply during CIGSe growth has been found to increase grain size. For example, the timing of NaF co-evaporation during a three-stage CIGSe growth has been shown to affect microstructure [29]. A comparative study of CIGSe absorbers grown on SLG with and without an alkali barrier layer blocking Na diffusion from the substrate during growth revealed that those with the barrier had smaller grains [39]. Additionally, CIGSe grown on fused silica substrates with extra Na exhibited increased grain size and columnar structure, highlighting the importance of Na supply during growth [28]. Previous studies have indicated that NaF PDT results in larger CIGSe grains compared with NaF co-evaporation, which produces smaller grains in the bulk due to higher Na concentration [36]. However, the exact influence of

Na on CIGS grain growth, especially beyond SLG substrates, is not well understood [22, 38, 44, 45]. In this work, we observed that Na from SLG significantly increases grain size notably on the surface compared with LNG, which is presumed to have minimal Na. Introducing additional Na via co-evaporation with 650 NaF yields optimal results and larger grains. However, increasing the NaF source temperature to 750°C reduces grain size, which may result from pronounced vertical GGI grading as observed in Figure 1c. Vertical GGI grading typically arises from limited Ga/In inter diffusion, leading to smaller grains, whereas minimal grading is associated with larger grain formation [42]. A similar trend of small grain formation with Na incorporation has been observed in CIGSe with steep Ga grading [29, 43]. The correlation between grain growth and Na depth profile, shown in Figure 1b, indicates that high Na concentration corresponds to regions with numerous grain boundaries, as seen in the SLG and 750 NaF absorbers. In contrast, 650 NaF, with fewer grain boundaries, shows lower Na concentration. This observation aligns with atomic probe tomography studies, which report an accumulation of Na at grain boundaries in CIGSe [46].

To investigate crystal quality, we analyzed the absorbers using X-ray diffraction (XRD). Figure 2b presents the fine scan normalized θ–2θ XRD patterns for the 112 reflex, with the full-width at half maximum (β) values displayed. The wide scan XRD pattern (10°–60°) is shown in Figure S5. All peaks correspond to the tetragonal chalcopyrite structure of CIGS (ICDD:00-056-1309). The β value is lowest for 650 NaF, indicating superior crystallinity, which is consistent with SEM observations. This relation of β values to grain size is also noticeable for LNG, SLG, and 750 NaF absorbers: Smaller grains in SEM correlate with larger β values. For 750 NaF, the peak becomes slightly asymmetric, and the 112 peak shifts to a higher angle, a trend also observed in the 700 NaF sample (Figure S5). This shift is attributed to unit cell deformation (out-of-plane), potentially caused by strain release from the Mo surface, similar to observations in CIGSe on GaAs substrates with Na_2Se PDT treatment [33]. In epitaxial CIGSe, a positive shift in the dominant 200 reflex after Na_2Se treatment is related to out-of-plane unit cell parameter changes due to strain release. In our polycrystalline CIGS, the positive shift is attributed to the release of strain caused by the Mo substrate with excess Na supply, which could explain the peeling effect observed with high (> 750°C) NaF concentrations. To further elucidate this strain effect, we measured XRD before and after exfoliating a CIGS absorber (without NaF co-evaporation) from the Mo back contact, as shown in Figure S5. After exfoliation, the Mo diffraction peak is absent, while the 112 CIGS peak shows a positive shift due to released strain. This effect is similar to that observed with the 750 NaF absorber, where excess Na accumulates on the Mo, releasing strain at the Mo/CIGS interface and impacting crystallization. A positive shift may also result from high Ga content due to lattice contraction from smaller Ga atoms partially occupying In lattice sites [7, 21, 47]. However, as Ga/In composition values are consistent on average across all absorbers, the positive shift is attributed primarily to the strain effect.

We employed PL and CL techniques to evaluate the effect of Na on the optoelectronic properties of CIGS absorbers. These techniques are instrumental in screening absorber quality and understanding defect nature before proceeding with complete solar cell fabrication [7, 13, 48]. Absolute PL measurements help predict the maximum V_{OC} and fill factor (FF) achievable in a completed solar cell [12, 13], while CL hyperspectral imaging can reveal the microscopic origins of recombination processes at the surface and across the absorber's depth [48, 49]. Figure 3a presents the normalized PL spectra of the absorbers under 1-sun equivalent photon flux, while Figure S6 shows the absolute PL spectra. The plan-view mean CL spectra of the absorbers are shown in Figure 3b. The E_g derived from the PL maximum (denoted as $E_{g(PL)}$), which corresponds to band-to-band (BB) radiative emission, is approximately 1.59 eV for LNG, SLG and 650 NaF, and 1.61 eV for 750 NaF, as shown in Figure 3c. Similarly, the CL maxima (denoted as $E_{g(CL)}$ corresponding to BB or near band edge emission (NBE)) are shown in Figure 3c. Both PL and CL show nearly the same E_g for all the absorbers, except for LNG. The differences in E_g, and defect emission, in LNG are attributed to inhomogeneities in the absorber. The absence of the dominant defect peak in CL is due to the significantly higher excitation intensity in CL compared with 1-sun PL. Higher excitation level makes the BB emission more prominent, as seen in the intensity-dependent PL spectra for LNG shown in Figure S6, where BB emission dominates with increasing excitation intensity. It is important to note that excitation with 1-sun equivalent photon flux and understanding of the corresponding electronic transitions are crucial for evaluating solar cell performance. Typically, $E_{g(PL)}$ is expected to correlate with the minimum band gap (the notch) of the absorber's depth profile and can be described quantitatively with respect to GGI ratio [1]. The samples SLG and 650 NaF are expected to have similar or closely matched notch band gaps, based on the GGI depth profile and ratios (Figure 1a,c), which is further confirmed by the energy of the PL maxima (Figure 3c). In contrast, the absorbers LNG and 750 NaF show the reverse trend in PL maximum energy than expected from the GGI profile. Here, LNG and 750 NaF show lower and higher E_g despite having higher and lower GGI at notch, respectively. In the case of the LNG absorber, this can be simply due to a shift of the PL maximum toward lower energies due to the high background from the defect luminescence and due to a shift of the emission energy due to tail states [13, 50]. The higher emission energy in the 750 NaF sample can indicate that the main emission is not coming from the notch, due to low mobility, which prevents the carriers from reaching the notch, or it could just be due to inhomogeneities of the sample. To further confirm, we excited the 750 NaF absorber with a low energy (660 nm) laser, which can penetrate deeper into the absorber, and observed a ~50 meV blueshift in $E_{g(PL)}$ as shown in Figure S6c. The observed blueshift arises not from carriers reaching the notch, but rather because carriers generated deeper in the absorber recombine before diffusing to the notch. As a result, the emission reflects local recombination from regions of higher bandgap, confirming limited carrier diffusion in the 750 NaF absorber. We note that, in 750 NaF, ΔE_F may overestimate the contribution to V_{OC} due to excitation depth differences between PL and sunlight.

LNG, with minimal Na, exhibits a broad deep defect (D_2) peak at lower energies (see log scale in Figure S6), as defined in [7], indicating predominant recombination through defect states [47]. In contrast, SLG, with sufficient Na, shows dominant BB emission along with a weak and shallow defect (D_1) around 1.4 eV, suggesting that the Na supply during CIGS growth

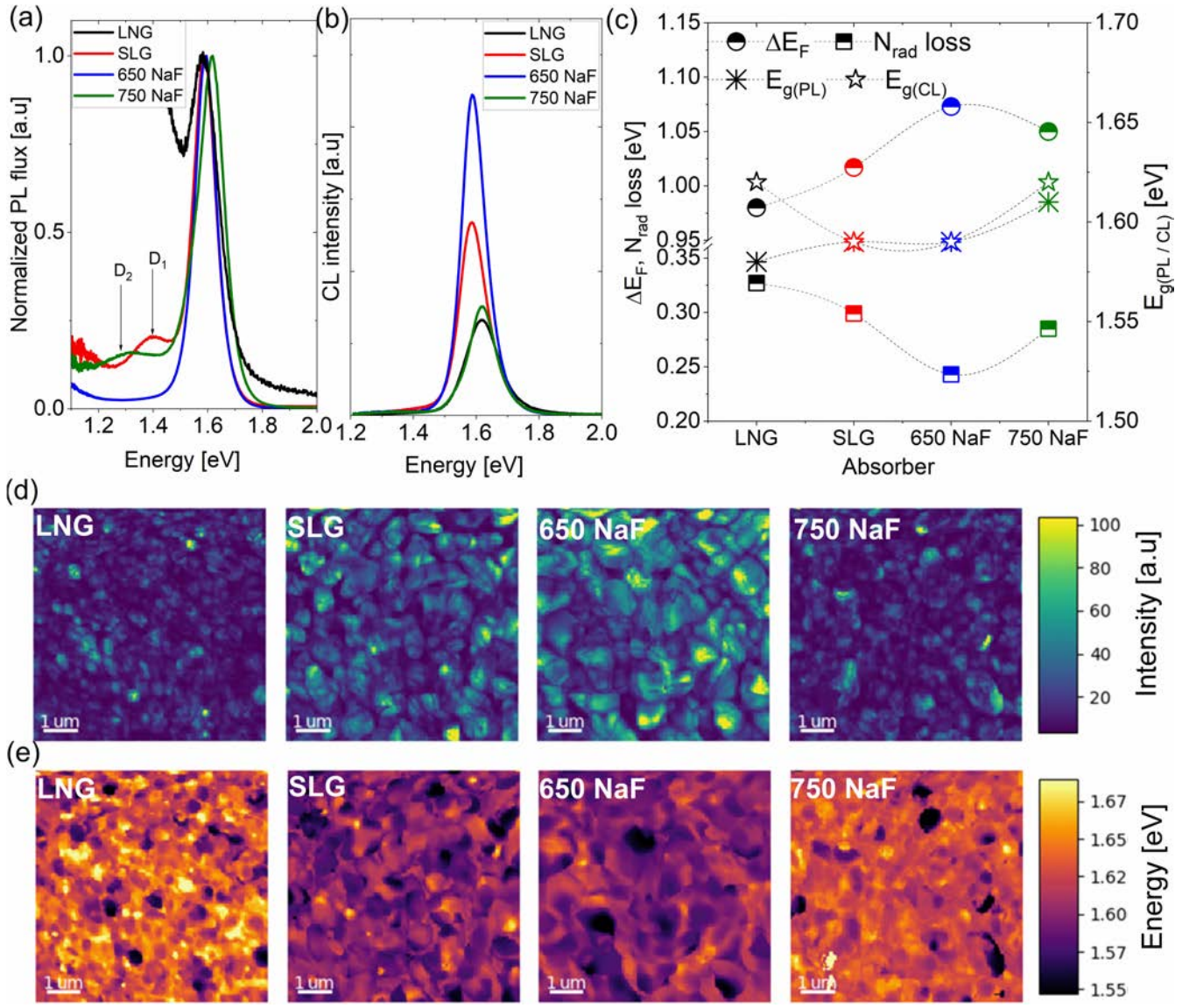

FIGURE 3 | Optoelectronic properties of CIGS with varying Na supply. (a) PL spectra, normalized to near band edge emission. (b) Plan-view mean CL spectra. (c) Optoelectronic parameters extracted from the 1 sun absolute PL measurements. The $E_{g(PL)}$ and $E_{g(CL)}$ for SLG and 650 NaF are overlapped on each other. (d) Panchromatic CL intensity maps and (e) NBE energy distribution maps of CIGS.

plays a critical role in reducing defects. The addition of 650 NaF further suppresses the D_1 defect, resulting in the highest PL quantum yield (Y_{PL}) among all absorbers. Absorbers with 600 and 700 NaF exhibit similar BB and D_1 peaks as SLG (Figures S6 and S7). However, 750 NaF leads to a detrimental D_2 emission below 1.3 eV, adversely affecting photovoltaic performance, as also here observed by the lower PL quantum yield [7]. The primary impact of these defects is non-radiative recombination, as indicated by the clear correlation between non-radiative losses and defect related emissions. The contribution of radiative losses through the defects is marginal: even in the LNG sample, BB emission still within the 10^{-2} range of the total radiative emission, whereas Y_{PL} drops below 10^{-5}. The mean CL spectra in Figure 3b reflect NBE intensity variations among different absorbers roughly consistent with PL results (see Figure S6). We used Y_{PL} approach, also called external radiative efficiency (ERE), to determine the quasi-Fermi level splitting ΔE_F as described in Ref [12]. The Y_{PL} was calculated using the relation, $Y_{PL} = \Phi_{PL}/\Phi_{laser}$, where Φ_{PL} represents an integrated flux of the BB emission peak between 1.45 and 2.0 eV, and $\emptyset_{laser}$ represents an incident photon flux corresponding to the number of photons in a 1-sun spectrum above the E_g. This approach neglects reflection of the laser on the sample surface and thus underestimates the Y_{PL} by about 20% [13]. The increase in Y_{PL} with 650 NaF demonstrates a reduction in non-radiative losses. The ΔE_F is determined using the relationship of the Shockley–Queisser V_{OC} limit and non-radiative recombination, as detailed in [51] and expressed in the following equation:

$$\Delta E_F = qV_{OC}^{SQ} + k_B T \times \ln Y_{PL} \quad (1)$$

where qV_{OC}^{SQ} is the SQ V_{OC} limit, k_B is the Boltzmann constant, and T is the temperature. The E_g for qV_{OC}^{SQ} is taken from $E_{g(PL)}$; however, we note that this approach further underestimates the ΔE_F by typically 10 to 20 meV [13]. The $E_{g(PL)}$, ΔE_F,

and non-radiative loss $\left(k_B T \times \ln Y_{\mathrm{PL}}\right)$ are shown in Figure 3c. The ΔE_F for the 650 NaF absorber is 1.07 eV, which is 60 meV higher than the reference SLG absorber, suggesting a potential for achieving high V_{OC} with an appropriate buffer layer [7, 10, 52]. We attribute the decrease in non-radiative losses (N_{rad} loss) from 299 meV (SLG) to 243 meV (650 NaF) to the suppression of bulk defects, as supported by the PL spectra, a crucial effect for highly efficient solar cells [10]. Conversely, the ΔE_F for the LNG-only absorber is 0.98 eV, reflecting defect-mediated recombination losses, underscoring the importance of adequate Na supply during CIGS growth. However, excess 750 NaF leads to decrease in ΔE_F due to an increase in non-radiative loss.

Figure 3d presents panchromatic plan view CL images of CIGS absorbers with different Na contents, LNG and 750 NaF show high-intensity emission from only a few grains, while 650 NaF exhibits a nearly uniform emission intensity across all grains with the overall highest intensity, consistent with PL results. CIGS on SLG shows uniform emission across grains but with lower total intensity. Dark regions in all maps indicate strongly inhibited radiative recombination in certain grains (notably high for LNG and 750 NaF) and at grain boundaries [7, 48, 53]. By fitting Gaussian functions to all peaks in each pixel of the maps, we can extract the emission energy of the peaks and investigate their variation across the probed area, as presented in Figure 3e. LNG is found to have a high NBE energy standard deviation of 27 meV, ranked the highest in all four samples. SLG and 650 NaF have a considerably lower standard deviation of the emission energy, at 19 and 18 meV, suggesting a much more uniform bandgap across the absorber surface. The NBE energy standard deviation for 750 NaF is 21 meV, which is much improved compared with LNG. Overall, these plan view CL results suggest that Na addition can enhance radiative recombination and improve compositional homogeneity.

To gain a deeper understanding of the emission energy and defect density variations across the depth of the absorbers, we performed microscopic mapping of their cross sections. Figure 4a shows the cross-sectional SE images of the absorbers used for hyperspectral CL mapping. Figure 4b provides panchromatic CL images showing the variation of the spectrally integrated intensity across the depth of the thin films. The mean CL spectra for cross-sectional CL are shown in Figure S8. LNG and SLG show strong emission intensity at the surface and at approximately 0.5 μm sub-surface, a depth we associate roughly with the position of the notch, based on the GDOES data in Figure 1c. The CIGS absorber with optimal Na supply (650 NaF) exhibits strong emission from the surface to around 0.3 μm depth, gradually fading toward the back contact. In contrast, 750 NaF shows poor intensity across the depth except at the position of the notch, with negligible emission at the surface, reflecting the higher defect concentration. Figure 4c shows the distribution of NBE emission energy across the cross-sectional map. The emission energy map shows that the area with the lowest emission energy—corresponding to the notch—is located close to the surface, with an emission energy of ~1.6 eV for all the absorbers, consistent with $E_{g(\mathrm{PL})}$ and $E_{g(\mathrm{CL})}$. A clear variation in emission energy is visible toward the back of the absorbers. The emission energy as a function of depth, extracted from a line scan in Figure 4c, is shown in Figure S9. The trend of increasing emission energy toward the back aligns with the GGI profile observed in GDOES, as discussed in Figure 1c. However, the high surface GGI observed in LNG is not detected in the CL depth profile, likely due to inhomogeneity within the absorber.

To get insight into the defect distribution, we map the intensity of the defect emission relative to the NBE emission intensity (Figure 4d). Note that the bright yellow areas at the

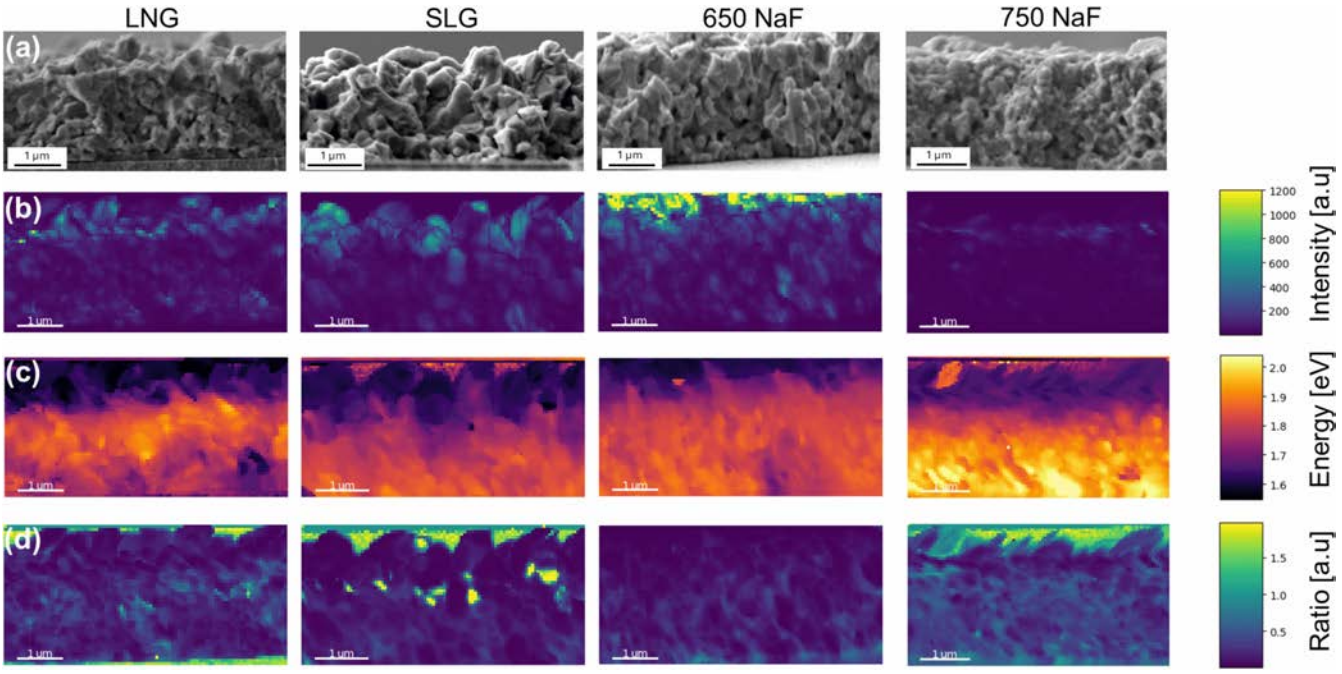

FIGURE 4 | Cross-sectional hyperspectral CL analysis of CIGS with different Na supply. (a) Secondary electron images used for mapping. (b) Panchromatic intensity images. (c) Emission energy distribution across the absorber depth. (d) Defect density, extracted as the ratio of defect intensity peak over NBE intensity peak. The scale bar in all images is 1 μm.

top of the maps are due to places, where the electron beam hits the empty space above the surface of the film not the actual cross section. These regions are artefacts that do not give information about the defect distribution. The LNG and even more the SLG film show spots with very high defect emission. In particular, in the SLG film, they seem to be located near the steepest gradient in the emission energy (see Figure 4c). All films besides the 650 NaF film show some defect emission near the surface, albeit reduced compared with the bulk. The 650 NaF film shows very low defect emission near the surface. It is likely that a low near-surface defect density contributes to a reduction in SCR recombination [53] and thus a lower diode factor in comparison with 750 NaF (see Table S3). Furthermore, the absence of surface defects helps to improve the translation of ΔE_F into actual V_{OC} [52]. It is worth noting that PL measurements average over these mapped surface areas; nonetheless, the local distribution of intensities and emission energies likely influences overall solar cell performances [54].

Additionally, we extracted spectra along the lines marked in Figure S10 to further understand emission energy variations across the depth, as shown in Figure 5a. It is worth noting that the line scan spectra integrated all the CL signals surrounded marker within 2.5 μm in width. The line spectra of LNG reveal jumps in the emission energy (best visible as peak broadening and splitting in the extracted spectra) near the notch position (marked with a red box). Jumps in the band gap, as opposed to a smooth gradient, were shown to be detrimental to absorber quality [55]. Additionally, LNG shows a band gap with lower bandgaps towards the back contact, which will certainly increase back contact recombination [17, 56, 57]. The lower bandgap near the back contact in the LNG sample is visible in many areas in the map in Figure 4c. Such a jump in the NBE emission energy near the notch position also can be observed in SLG and 650 NaF sample. No clear reverse bandgap gradient in the middle or lower part of the absorber has been found in the line spectra of SLG and 650 NaF. One area shown in the map in Figure 4c exhibited a reverse gradient, which may be caused by local inhomogeneity. 750 NaF has the smoothest emission energy transition around the notch position with only subtle NBE peak change, but it, overall, has the largest energy change from the frontside to the backside (agreeing with the GDOES measurements). Similar to the observation in the top view CL maps, a moderate amount of Na addition can improve overall compositional uniformity. In Figure 4c, we can also see pronounced variations in emission energy across the film, corresponding to regions of higher and lower gallium content. In Figure S11, we show another set of line spectra, averaging over a much narrower region (0.5 μm). These spectra show distinct jumps in emission energy with depth, and double emission peaks in places where regions of more than one composition are being sampled. This also illustrates the simultaneous existence of regions of higher and lower gallium content, consistent with previous observations in [55]. This indicates that further process optimization is needed to grow phase pure CIGS.

Increased quasi-Fermi level splitting can be due to longer minority carrier lifetimes and due to higher doping [12]. Time-resolved

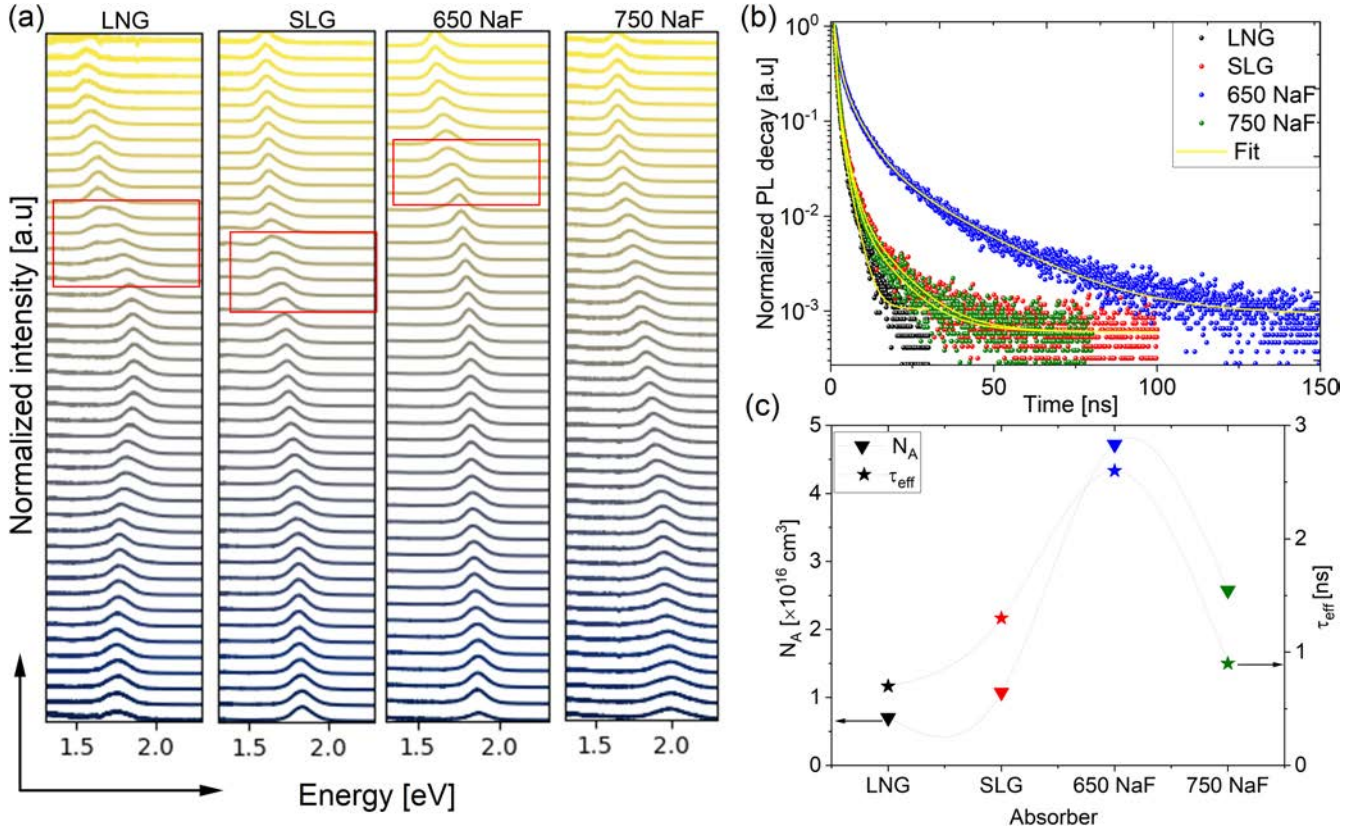

FIGURE 5 | (a) Cross-sectional CL line scan of CIGS with varying Na supply, showing variation in spectra across the depth. (b) TRPL transients and (c) calculated doping density alongside effective lifetime of CIGS with different Na supply.

photoluminescence (TRPL) spectroscopy gives an indication of changes in minority carrier lifetime. Figure 5b presents the TRPL transients for the absorbers, measured at the lowest excitation intensity possible to ensure that we measure minority carrier lifetimes. The decays are not mono-exponential; therefore, we fit them with a tri-exponential fit (a bi-exponential fit for LNG). The fitted values for the TRPL transients are summarized in Table S2. The long-lifetime component ($\boldsymbol{\tau}_3$) of the TRPL transients, which accounts for both surface and bulk recombination, is notably high for the 650 NaF-based CIGS, reaching up to 20.6 ns. This feature indicates a longer carrier lifetime and potentially improved charge extraction efficiency. The effective carrier lifetime ($\boldsymbol{\tau}_{\text{eff}}$), representing the weighted average of time constants, is calculated using the relation described in Equation (2) [58],

$$\boldsymbol{\tau}_{\text{eff}} = \frac{\sum A_i \boldsymbol{\tau}_i}{\sum A_i} \tag{2}$$

where the A_i are the amplitudes of the different lifetimes $\boldsymbol{\tau}_i$, $i = 1, 2, 3$. The $\boldsymbol{\tau}_{\text{eff}}$ is plotted in Figure 5c. $\boldsymbol{\tau}_{\text{eff}}$ is considerably smaller than long decay time ($\boldsymbol{\tau}_2$ or $\boldsymbol{\tau}_3$, see Table S2) for all samples, because it also contains the fast decay processes at the beginning of the decay. However, they both show the same trends. The long decay time for LNG is 2.4 ns, which increases to 9.7 ns for SLG. The optimal 650 NaF further increases the $\boldsymbol{\tau}_3$ to 20.6 ns, while the excess 750 NaF declines the $\boldsymbol{\tau}_3$ to 9.0 ns. The short decay time ($\boldsymbol{\tau}_1$) observed in all the absorbers is attributed to the charge carrier separation at the surface or trapping [58, 59]. Charge carrier dynamics in CIGS have not been extensively explored in literature, with only a few recent reports providing insights [7, 16]. For instance, previous work from our laboratory demonstrated a long decay time of 3.2 ns, which improved to 4.5 ns with the addition of a buffer layer [7]. The notably long decay ($\boldsymbol{\tau}_3$), without buffer layer, observed in this study for CIGS with 650 NaF is attributed to reduced non-radiative losses, a lower defect density across the absorber's depth, and an increased grain size. To gain a deeper understanding of the different contributions to the increase in ΔE_F, we calculated the hole doping density (N_A) using the relationship between electron Fermi level and lifetime on the one side and hole Fermi level and doping density on the other side (see e.g. [16]), as described by Equation (3),

$$N_A = p_0 = \frac{d.N_C N_v}{G.\boldsymbol{\tau}_3} exp\left(\frac{\Delta E_F - E_g}{k_B T}\right) \tag{3}$$

where N_c and N_v are the effective density of the states of the conduction and valance band, where we use the values for $CuInS_2$ [15] as it is closeset available, and Ga content is consistent on average across all the absorbers. G is the generation flux during steady state ΔE_F measurement, and d is the thickness of the film (~2.8 μm from cross sectional SEM, see Figure 4). The calculated doping density is presented in Figure 5c. The N_A for the LNG absorber is $7.0 \times 10^{15}\,\text{cm}^{-3}$, which increases to $1.08 \times 10^{16}\,\text{cm}^{-3}$ in the SLG grown absorber. The optimal Na supply from 650 NaF further enhances the N_A to $4.7 \times 10^{16}\,\text{cm}^{-3}$. However, with higher 750 NaF supply, the N_A decreases to $2.5 \times 10^{16}\,\text{cm}^{-3}$. The observed trend in doping concentration is consistent with findings from various studies on chalcopyrite absorbers grown with an alkali barrier and controlled Na supply [23, 25, 38]. Analysis of the best-case scenario for SLG and 650 NaF absorbers reveals that a ~0.6 fold increase in N_A and a ~2 ns increase in long decay time contributes to a ~10 meV improvement in ΔE_F, considering the same E_g.

One of the reasons for the variation in hole doping density could be attributed to the Na out diffusion process during CIGS growth, as theoretically observed in selenide chalcopyrite [32]. The available Na supply during the CIGS growth promotes the formation of Na_{Cu} impurities, due to its low formation energy (0.55 eV) relative to Cu in the chalcopyrite structure. However, Na_{Cu} is thermodynamically unstable, and Na migrates out of the grains with a migration energy of 0.36 eV at room temperature [60], leaving behind Cu vacancies, which results in an increased N_A. This phenomenon, however, is not fully understood in the context of high Na concentrations within the grains, as we observe a decrease in N_A with increasing Na supply. The decrease in N_A with excess NaF could be linked to the poor quality of the absorber, as discussed earlier. It is important to note that the optimal NaF concentration has a very narrow window. For instance, with 600 and 700 NaF, the Na supply is either below or above the optimal range, necessitating precise optimization depending on experimental conditions. This narrow window is due to the significant variation in NaF evaporation rate with every 20°C change in source temperature.

Finally, we fabricated the solar cells incorporating a ~50-nm-thick $ZnSnO_x$ buffer layer, deposited using atomic layer deposition, in combination with a sputtered $(Zn,Mg)O_x$ i-layer, to avoid barriers for the forward current and FF losses [19]. Thus, the device configuration is given by Mo/CIGS/$ZnSnO_x$/$(Zn,Mg)O_x$/Al:ZnO/MgF_2 as illustrated in Figure 6a. The top three layers (from top to bottom) function as an antireflection coating, a transparent front contact, and an intrinsic layer, respectively. Additionally, some unintentional variations in the buffer layer composition, particularly in the [Sn]/([Sn] + [Zn]) ratio, were observed due to gas flow interruptions on the surface of the NaF co-evaporated CIGS. The [Sn]/([Sn] + [Zn]) ratios for devices based on LNG and SLG substrates were 0.19, measured on reference SLG pieces within the deposition chamber, while for NaF 650 and NaF 750, the ratios were 0.15. Figure 6b presents the active area current density-voltage (J-V) curves under dark and illuminated conditions, and Figure 6c displays the external quantum efficiency (EQE) alongside the integrated short-circuit current density (J_{SC}) of the best performing solar cells. The corresponding photovoltaic parameters (J_{SC}, V_{OC}, FF, and PCE) are summarized in Table 1. The PCE was calculated based on the integrated J_{SC} extracted from the EQE spectrum; this is the preferred approach, owing to the spectral mismatch of the halogen lamp used in the solar simulator. Furthermore, the dark I–V curves were fitted using the standard one-diode and two-diode models and the corresponding series resistance, shunt resistance, diode factor, and dark current values are summarized in Table S3. The 650 NaF-based solar cell shows reduced series resistance and diode factor in comparison with the 750 NaF solar cell.

The interfacial loss (IF_{loss}), determined from the difference between the ΔE_F and V_{OC}, is shown in Figure 6d. The solar cell fabricated on the LNG substrate exhibited poor performance, as

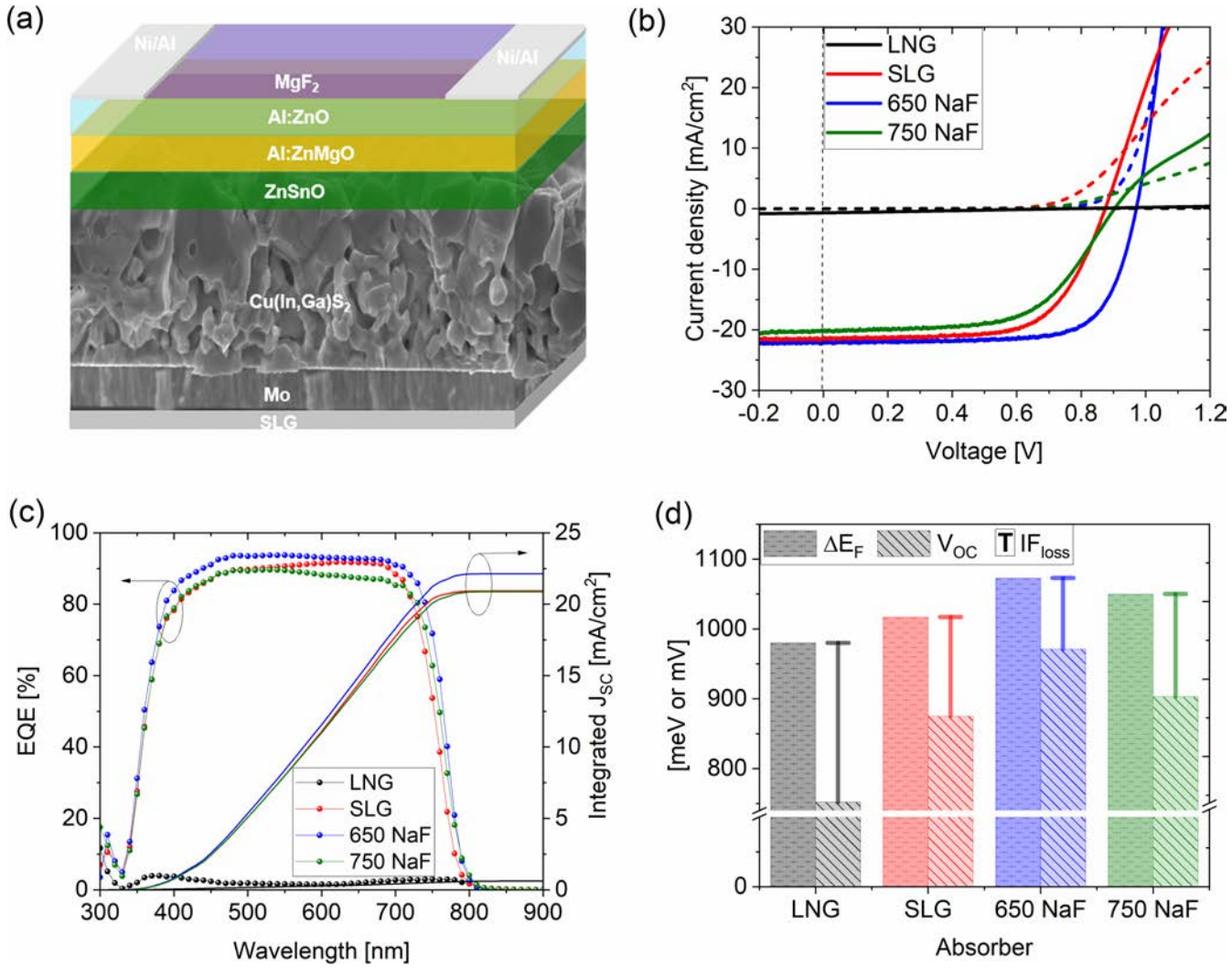

FIGURE 6 | Photovoltaic performance of the CIGS solar cell with varying Na supply. (a) Schematic of the solar cell structure with cross-sectional SEM image of 650 NaF absorber. (b) Active area J–V curves under dark and illuminated conditions. (c) EQE spectra alongside integrated J_{SC}. (d) interfacial loss determined from the difference between ΔE_F and V_{OC}.

TABLE 1 | Photovoltaic parameters V_{OC}, J_{SC}, FF, and PCE of the best CIGS solar cells with varied Na supply during the growth. The PCE values were calculated based on both $J_{SC(EQE)}$ and $J_{SC(JV)}$ are provided.

Absorber	V_{OC} (mV)	$J_{SC(EQE)}$ (mA/cm^2)	$J_{SC(J\text{-}V)}$ (mA/cm^2)	FF (%)	$PCE_{(EQE)}$ (%)	$PCE_{(J\text{-}V)}$ (%)
LNG	752	0.6	0.4	27.2	0.1	0.1
SLG	875	20.9	21.3	66.2	12.1	12.3
650 NaF	971	22.1	22.0	73.1	15.7	15.7
750 NaF	903	20.9	20.2	59.9	11.3	10.9

anticipated from the 1-sun PL spectrum and defect density map from CL mapping. Despite all parameters being suboptimal for the LNG device, a reasonable V_{OC} of 752 meV was obtained. The J_{SC} however is almost nonexistent. The best solar cell based on SLG delivered a PCE of 12.1% with a V_{OC} of 875 meV. Despite the high ΔE_F, defects at or near the surface lead to increased non-radiative recombination and a gradient in the electron quasi-Fermi level, resulting in a lower V_{OC} [52]. We note that, the performance of the SLG-based device could be less optimal compared with other NaF co-evaporated devices, based on the different [Sn]/([Sn] + [Zn]) ratios, which likely cause differences in the band alignment. As anticipated from the optoelectronic and structural characterization results, the 650 NaF-based solar cell emerged as the champion, delivering a high V_{OC} of 971 meV with an FF of 73.1%, resulting in an active area PCE of 15.7%. Furthermore, in the optimal 650 NaF device, the interface deficit was significantly decreased to 102 meV. Our previous work has shown that further buffer optimization can reduce this

deficit further [7]. However, increasing the Na supply to 750 NaF proved detrimental to solar cell performance, despite yielding a better V_{OC} than the SLG-based device. The increased V_{OC} deficit in the 750 NaF device, compared with the 650 NaF device, is possibly due to surface defect density. The drop in PCE is mainly attributed to the poor FF and J_{SC}, as widely observed in CIGSe with excess Na [35, 40]. The kink observed in the J-V curve is indicative of a potential barrier at the interface, which likely results from non-optimized band alignment, indicating once more the need for further buffer optimization [19, 61]. This barrier can also cause voltage-dependent carrier collection and maybe the explanation of the reduced EQE and J_{SC} [19]. In the case of the 750 NaF-based solar cell, the kink is more pronounced, suggesting that the interface barrier may be more significant, thereby contributing to reduced FF and overall efficiency. The average values of the photovoltaic parameters follow the same trends as those of the best cells. Figure S12 shows the statistical distribution of photovoltaic parameters from eight devices (four for LNG). For 650 NaF, the solar cells exhibit a narrow distribution of photovoltaic parameters, indicating better homogeneity and absorber quality.

The E_g values extracted from the inflection point of the EQE spectra for all absorbers are presented in Figure S13. The EQE spectrum for LNG was poor and is therefore excluded from further discussion. Compared with the CIGS with 650 NaF, the SLG sample shows lower EQE across the wavelength (λ) range of 400–720 nm, indicating a lower collection function near the front surface. This could be due to low doping [19] and a large SCR, which would shift the p-n point far into the absorber and make holes minority carriers near the front interface [56]. The decreased EQE for 750 NaF, compared with 650 NaF, may be due to voltage-dependent carrier collection due to a barrier. Figure S13 shows the voltage-dependent EQE spectra of the solar cells. The carrier collection remains unaffected under negative bias for all the solar cells. However, a significant reduction is observed under positive bias for the SLG and 750 NaF-based solar cells, while 650 NaF solar cells show relatively minimal reduction. The unaffected shape of the EQE spectra indicates that the carrier collection loss is independent of wavelength. However, electrical J_{SC} losses are more pronounced in SLG and 750 NaF solar cells. In summary, optimizing NaF supply during CIGS growth is crucial for suppressing surface and bulk defects, which is essential for achieving highly efficient solar cells with optimally band-aligned buffer layers.

3 | Conclusions

In this study, we have elucidated the critical role of additional Na supply in optimizing the performance of wide bandgap CIGS photovoltaic absorbers. By combining Na from the glass substrate with NaF co-evaporation, we demonstrated that optimal Na supply enhances Ga/In interdiffusion, reduces lateral bandgap fluctuations, and promotes the formation of larger grains with superior crystallinity. An absolute 1 sun calibrated PL measurements reveal that optimal Na leads to a significant reduction in non-radiative losses, resulting in a high ΔE_F of 1.07 eV and a long carrier decay time of 20.6 ns. Cross-sectional CL hyperspectral mappings further indicate that reducing defect density at the surface and SCR is crucial for effectively translating ΔE_F into a high V_{OC}. The champion wide bandgap solar cell fabricated with 650 NaF CIGS achieved an active area PCE of 15.7% and a V_{OC} of 971 meV, underscoring the importance of precise Na management for achieving high-performance CIGS solar cells.

4 | Experimental Section

The CIGS absorbers were grown using a well-established three-stage process previously described for both sulfide and selenide chalcopyrite [7, 57, 62]. We used Molybdenum (Mo) coated soda-lime glass substrates (SLG) and low Na glass (LNG) substrate. The actual substrate temperatures (T_S) were ~470°C during the first stage and ~600°C during the second and third stages, with a ramp rate of 20°C/min and substrate rotation at 4 rpm. The actual substrate temperature was estimated based on the substrate heater calibration using a pyrometer. The schematic representation of the three-stage process is provided in Figure S1. Before evaporation, the Mo surface was cleaned at T_S of 450°C for 15 min followed by exposure to sulfur vapor at T_S of 400°C for 15 min, likely resulting in the formation of a MoS_2 layer, although its thickness remains undetermined. In the first stage, calibrated fluxes of gallium (Ga) and indium (In) were co-evaporated under a sulfur partial pressure ranging between 2×10^{-5} mbar and 8×10^{-5} mbar. In the second stage, calibrated fluxes of copper (Cu) and sodium fluoride (NaF) were co-evaporated. NaF in all the absorbers was co-evaporated for 45 min regardless of Cu evaporation time (usually 50 to 60 min). NaF was introduced in the second stage to promote favorable Na incorporation such as Na_{Cu}. Once a Cu-rich stoichiometry was formed (~7.5% excess), monitored by an increase in heating power and pyrometer readout, Ga and In were co-evaporated again (with no Cu) in the third stage to form a Cu-poor stoichiometry, with the Ga flux being lower than in the first stage [57]. Various batches of CIGS were grown by varying the NaF source temperature between 600, 650, 700, and 750°C [29, 36]. All the NaF co-evaporated CIGS absorbers were deposited on SLG substrates. The $ZnSnO_x$ buffer layer was deposited in an F120 Microchemistry ALD reactor at 120°C using a metal–organic precursor/N_2-purge/H_2O/N_2-purge cycle with the pulse and purge times of 0.4/0.8/0.4/0.8 s respectively. The metal–organic precursor tetrakisdimethyl-amino-Sn (TDMASn) was heated to 40°C in a bubbler source using N_2 carrier gas, whereas the other metal–organic precursor diethyl-zinc (DEZ) and H_2O were effused into the reactor due to their high vapor pressures at room temperature. The $ZnSnO_x$ process used a five-cycle supercycle, where the metal–organic precursor for each cycle was altered in the following sequence: DEZ, DEZ, TDMASn, DEZ, and TDMASn. This supercycle scheme resulted in a [Sn]/([Sn] + [Zn]) ratio of 0.18 for the $ZnSnO_x$ film, except for the process run where the gas flow was disrupted, which led to a ratio of 0.15. The supercycle was repeated 300 times using a total of 1500 cycles, which resulted in a $ZnSnO_x$ film thickness of about 50–60 nm. This was followed by an Al:MgZnO window layer and an Al:ZnO transparent front contact, both deposited by magnetron sputtering. The device was completed with an evaporated Ni/Al grid electrode, topped with an ~100-nm-thick MgF_2 antireflection coating. Individual cells are defined by mechanical scribing with an active area of ~0.42 cm^2.

5 | Characterizations

The chemical compositions were analyzed by EDS at operating voltages of 7 and 20 kV. The compositional depth profiles were recorded by glow discharge optical emission spectroscopy (GDOES). An argon plasma at a pressure of 450 Pa erodes the sample and generates a light emission of the sputtered atoms. The specific emission lines of the single elements are optically diffracted and detected by several photomultipliers. For the quantification of the CIGS matrix elements, the reference measurement by EDS was used. The sodium concentration is determined by a relative sensitivity factor (RSF), which was calculated from implanted reference samples.

The cross-sectional morphology of the absorbers was examined using SEM. Structural characterization was conducted through XRD utilizing Cu-Kα radiation, and the data were plotted without applying instrumental resolution correction.

The quasi-Fermi level splitting (ΔE_F) measurements on the bare absorbers were performed by a home-built absolute PL setup equipped with a 405-nm laser excitation source at room temperature using a CCD Si detector [12]. The experimental setup is first calibrated, and the resulting spectra are corrected spectrally and in intensity, as described in ref. [55]. The incident photon flux has been set to match the 1-sun photon flux that an absorber of E_g 1.6 eV would receive under an AM 1.5 illumination. The PL quantum yield (Y_{PL}) method was used to determine the ΔE_F using the PL maximum as the band gap [12, 13] and explained in the PL section.

The CL measurements were performed using an Attolight Allain 4027 Chronos dedicated CL-SEM at room temperature. All CL maps were acquired with 5 kV beam acceleration voltage, 1.25 nA measurement current, and a 50 μm aperture. The exposure time per pixel for all maps was 500 ms. The interaction volume under the current setting estimated by Monte Carlo Casino has an extent of about 150 nm. The CL data analysis was carried out using Hyperspy and Lumispy [63, 64]. For the extraction of NBE and defect peak features, such as peak energy, intensity, and full-width-half-maximum, two Gaussian peaks were applied during fitting.

The TRPL measurements were performed using a time-correlated single photon counting (TCSPC) system with a 638-nm pulsed laser operating at a repetition rate of 5 MHz. The band edge emission was detected with a bandwidth of 46 nm.

The solar cells were characterized using a class AAA solar simulator calibrated with a reference standard Si solar cell (RQN3154). Current–voltage (I-V) measurements were performed at room temperature in the forward direction using an IV source measure unit, with a scan speed of 50 mV/s. The active solar cell area, approximately 0.42 cm^2, was determined using a Leica microscope and the ImageJ software. The active area is given by the outer circumference of the scribed cell minus the area of the metal grids. The entire active area was illuminated with 1 sun (100 mW/cm^2) during the measurements without using any mask. The EQE of the solar cells was measured using chopped illumination from a halogen-xenon lamp (Xenon short arc lamp, Ushio UXL-302-0) and a lock-in amplifier to detect the photocurrent.

Author Contributions

A.V and S.S. conceived ideas, designed experiments, and wrote the first draft of the manuscript. S.S. was responsible for funding acquisition and project supervision. A.V prepared samples and performed PL measurements, optoelectronic analyses, XRD, EDX characterizations, device fabrication and electrical measurements. K.K contributed to sample preparation and device characterization. M.M. contributed to SEM imaging, window and contact layers deposition. A.J.M.P and S.G contributed to PL and TRPL measurements. Y.H, G.K and R.O performed and analysis CL measurements. A.H and T.T contributed to buffer layer deposition. W.H and W.W Performed GDOES measurements. All authors participated in the discussion of data and results, and reviewed and edited the draft of the manuscript.

Acknowledgements

This work was funded by the Luxembourgish Fond National de la Recherche (FNR) for REACH (Project no: INTER/UKRI/20/15050982) and the European Union within the SITA project (no. 101075626). The Cambridge team would like to acknowledge funding from the EPSRC under EP/V029231/1 and EP/R025193/1. For the purpose of open access, the author has applied a Creative Commons Attribution 4.0 International (CC BY 4.0) license to any Author Accepted manuscript version arising from this submission. Views and opinions expressed are however those of the author(s) only and do not necessarily reflect those of the European Union or CINEA. Neither the European Union nor the granting authority can be held responsible for them. We thank Thomas Schuler for the technical support and Dr. Damilola Adeleye for the discussion on the absorber growth.

Funding

This work was funded by Luxembourgish Fond National de la Recherche (FNR) for REACH (Project no: INTER/UKRI/20/15050982) and European Union within the SITA project (no. 101075626).

Data Availability Statement

The data that support the findings of this study are available from the corresponding author upon reasonable request.

References

1. I. V. Bodnar and A. I. Lukomskii, "The Concentration Dependence of the Band Gap for $CuGa_xIn_{1-x}S_2$ and $AgGa_xIn_{1-x}S_2$ Solid Solutions," *Physica Status Solidi (A)* 98 (1986): K165–K169.

2. M. Powalla, S. Paetel, D. Hariskos, et al., "Advances in Cost-Efficient Thin-Film Photovoltaics Based on $Cu(In,Ga)Se_2$," *Engineering* 3 (2017): 445–451.

3. J. S. S. B. H. King, D. Riley, C. B. Jones, and C. D. Robinson, "Degradation Assessment of Fielded CIGS Photovoltaic Arrays," in *44th Photovoltaic Specialist Conference (PVSC)* (IEEE, 2017), 3155.

4. F. Karg, "High Efficiency CIGS Solar Modules," *Energy Procedia* 15 (2012): 275–282.

5. S. Niki, M. Contreras, I. Repins, et al., "CIGS Absorbers and Processes," *Progress in Photovoltaics: Research and Applications* 18 (2010): 453–466.

6. H. Hiroi, Y. Iwata, S. Adachi, H. Sugimoto, and A. Yamada, "New World-Record Efficiency for Pure-Sulfide $Cu(In,Ga)S_2$ Thin-Film Solar Cell With Cd-Free Buffer Layer via KCN-Free Process," *IEEE Journal of Photovoltaics* 6 (2016): 760–763.

7. S. Shukla, M. Sood, D. Adeleye, et al., "Over 15% Efficient Wide-Band-Gap $Cu(In,Ga)S_2$ Solar Cell: Suppressing Bulk and Interface

Recombination Through Composition Engineering," *Joule* 5 (2021): 1816–1831.

8. N. Barreau, E. Bertin, A. Crossay, et al., "Investigation of Co-Evaporated Polycrystalline Cu(In,Ga)S_2 Thin Film Yielding 16.0% Efficiency Solar Cell," *EPJ Photovoltaics* 13 (2022): 17.

9. J. Keller, K. Kiselman, O. D. Gargand, et al., "High-Concentration Silver Alloying and Steep Back-Contact Gallium Grading Enabling Copper Indium Gallium Selenide Solar Cell With 23.6% Efficiency," *Nature Energy* 9 (2024): 467–478.

10. S. Siebentritt, A. Lomuscio, D. Adeleye, M. Sood, and A. Dwivedi, "Sulfide Chalcopyrite Solar Cells–Are They the Same as Selenides with a Wider Bandgap?," *physica status solidi (RRL) – Rapid Research Letters* 16 (2022): 2200126.

11. H. Hiroi, Y. Iwata, H. Sugimoto, and A. Yamada, "Progress Toward 1000-mV Open-Circuit Voltage on Chalcopyrite Solar Cells," *IEEE Journal of Photovoltaics* 6 (2016): 1630–1634.

12. S. Siebentritt, T. P. Weiss, M. Sood, M. H. Wolter, A. Lomuscio, and O. Ramirez, "How Photoluminescence Can Predict the Efficiency of Solar Cells," *Journal of Physics: Materials* 4 (2021): 042010.

13. S. Siebentritt, U. Rau, S. Gharabeiki, et al., "Photoluminescence Assessment of Materials for Solar Cell Absorbers," *Faraday Discussions* 239 (2022): 112–129.

14. F. Babbe, L. Choubrac, and S. Siebentritt, "Quasi Fermi Level Splitting of Cu-Rich and Cu-Poor Cu(In,Ga)Se_2 Absorber Layers," *Applied Physics Letters* 109 (2016): 082105.

15. A. Lomuscio, T. Rodel, T. Schwarz, et al., "Quasi-Fermi-Level Splitting of Cu-Poor and Cu-Rich $CuInS_2$ Absorber Layers," *Physical Review Applied* 11 (2019): 054052.

16. D. Adeleye, A. Lomuscio, M. Sood, and S. Siebentritt, "Lifetime, Quasi-Fermi Level Splitting and Doping Concentration of Cu-Rich $CuInS_2$ Absorbers," *Materials Research Express* 8 (2021): 025905.

17. T. Wang, F. Ehre, T. P. Weiss, et al., "Diode Factor in Solar Cells With Metastable Defects and Back Contact Recombination," *Advanced Energy Materials* 12 (2022): 2202076.

18. L. Weinhardt, O. Fuchs, D. Groß, et al., "Band Alignment at the CdS/Cu(In,Ga)S_2 Interface in Thin-Film Solar Cells," *Applied Physics Letters* 86 (2005): 062109.

19. M. Sood, P. Gnanasambandan, D. Adeleye, et al., "Electrical Barriers and Their Elimination by Tuning (Zn,Mg)O Buffer Composition in Cu(In,Ga)S_2 Solar Cells: Systematic Approach to Achieve Over 14% Power Conversion Efficiency," *Journal of Physics. Energy* 4 (2022): 045005.

20. H. Hiroi, Y. Iwata, K. Horiguchi, and H. Sugimoto, "960-mV Open-Circuit Voltage Chalcopyrite Solar Cell," *IEEE Journal of Photovoltaics* 6 (2016): 309–312.

21. A. Thomere, N. Barreau, N. Stephant, et al., "Formation of Cu(In,Ga)S_2 Chalcopyrite Thin Films Following a 3-Stage Co-Evaporation Process," *Solar Energy Materials and Solar Cells* 237 (2022): 111563.

22. B. Marsen, H. Wilhelm, L. Steinkopf, et al., "Effect of Copper-Deficiency on Multi-Stage Co-Evaporated Cu(In,Ga)S_2 Absorber Layers and Solar Cells," *Thin Solid Films* 519 (2011): 7224–7227.

23. M. A. Contreras, B. Egaas, P. Dippo, et al., "On the Role of Na and Modifications to Cu(In,Ga)Se_2 Absorber Materials Using Thin-MF (M=Na, K, Cs) Precursor Layers," in *26th IEEE Photovoltaic Specialists Conference* (IEEE, 1997), 359–362.

24. J. Hedstrom, H. Ohlsen, M. Bodegard, et al., "ZnO/CdS/Cu(In,Ga)Se_2 Thin Film Solar Cells With Improved Performance," in *Conference Record of the Twenty Third IEEE Photovoltaic Specialists Conference, Anaheim, CA, USA - 1993 (Cat. No.93CH3283-9)* (IEEE, 1993), 364–371.

25. M. Ruckh, D. Schmid, M. Kaiser, R. Schäffler, T. Walter, and H. W. Schock, "Influence of Substrates on the Electrical Properties of Cu(In,Ga)Se_2 Thin Films," *Solar Energy Materials and Solar Cells* 41-42 (1996): 335–343.

26. D. Rudmann, A. F. De Cunha, M. Kaelin, et al., "Efficiency Enhancement of Cu(In,Ga)Se_2 Solar Cells due to Post-Deposition Na Incorporation," *Applied Physics Letters* 84 (2004): 1129–1131.

27. P. M. P. Salomé, A. Hultqvist, V. Fjällström, et al., "Incorporation of Na in Cu(In,Ga)Se_2 Thin-Film Solar Cells: A Statistical Comparison Between Na From Soda-Lime Glass and From a Precursor Layer of NaF," *IEEE Journal of Photovoltaics* 4 (2014): 1659–1664.

28. V. Probst, J. Rimmasch, W. Riedl, et al., "The Impact of Controlled Sodium Incorporation on Rapid Thermal Processed Cu(InGa)Se_2 Thin Films and Devices," in *Proceedings of IEEE 1st World Conference on Photovoltaic Energy Conversion*, vol. 1 (IEEE, 1994), 144–147.

29. D. Güttler, A. Chirila, S. Seyrling, et al., "Influence of NaF Incorporation During Cu(In,Ga)Se_2 Growth on Microstructure and Photovoltaic Performance," in *35th IEEE Photovoltaic Specialists Conference* (IEEE, 2010), 3420–3424.

30. S.-H. Wei, S. B. Zhang, and A. Zunger, "Effects of Na on the Electrical and Structural Properties of $CuInSe_2$," *Journal of Applied Physics* 85 (1999): 7214–7218.

31. A. Rockett, "The Effect of Na in Polycrystalline and Epitaxial Single-Crystal $CuIn_{1-x}Ga_xSe_2$," *Thin Solid Films* 480-481 (2005): 2–7.

32. Z. K. Yuan, S. Chen, Y. Xie, et al., "Na-Diffusion Enhanced p-Type Conductivity in Cu(In,Ga)Se_2: A New Mechanism for Efficient Doping in Semiconductors," *Advanced Energy Materials* 6 (2016): 1601191.

33. D. Colombara, F. Werner, T. Schwarz, et al., "Sodium Enhances Indium-Gallium Interdiffusion in Copper Indium Gallium Diselenide Photovoltaic Absorbers," *Nature Communications* 9 (2018): 826.

34. S. Siebentritt, E. Avancini, M. Bär, et al., "Heavy Alkali Treatment of Cu(In,Ga)Se_2 Solar Cells: Surface Versus Bulk Effects," *Advanced Energy Materials* 10 (2020): 1903752.

35. W. Thongkham, A. Pankiew, K. Yoodee, and S. Chatraphorn, "Enhancing Efficiency of Cu(In,Ga)Se_2 Solar Cells on Flexible Stainless Steel Foils Using NaF Co-evaporation," *Solar Energy* 92 (2013): 189–195.

36. B. Bissig, P. Reinhard, F. Pianezzi, et al., "Effects of NaF Evaporation During Low Temperature Cu(In,Ga)Se_2 Growth," *Thin Solid Films* 582 (2015): 56–59.

37. F. Babbe, N. Nicoara, H. Guthrey, et al., "Vacuum-Healing of Grain Boundaries in Sodium-Doped $CuInSe_2$ Solar Cell Absorbers," *Advanced Energy Materials* 13 (2023): 2204183.

38. R. Kaigawa, Y. Satake, K. Ban, S. Merdes, and R. Klenk, "Effects of Na on the Properties of Cu(In,Ga)S_2 Solar Cells," *Thin Solid Films* 519 (2011): 5535–5538.

39. M. Bodeg Ård, K. Granath, and L. Stolt, "Growth of Cu(In,Ga)Se_2 Thin Films by Coevaporation Using Alkaline Precursors," *Thin Solid Films* 361–362 (2000): 9–16.

40. D. H. Cho, Y. D. Chung, K. S. Lee, J. H. Kim, S. J. Park, and J. Kim, "Control of Na Diffusion From Soda-Lime Glass and NaF Film Into Cu(In,Ga)Se_2 for Thin-Film Solar Cells," in *IEEE 38th Photovoltaic Specialists Conference (PVSC) PART 2* (IEEE, 2012), 1–4.

41. M. A. Contreras, J. Tuttle, A. Gabor, et al., "High Efficiency Graded Bandgap Thin-Film Polycrystalline Cu(In,Ga)Se_2-Based Solar Cells," *Solar Energy Materials and Solar Cells* 41–42 (1996): 231–246.

42. L. Chen, J. Lee, and W. N. Shafarman, "The Comparison of (Ag,Cu)(In,Ga)Se_2 and Cu(In,Ga)Se_2 Thin Films Deposited by Three-Stage Co-evaporation," *IEEE Journal of Photovoltaics* 4 (2014): 447–451.

43. D. Rudmann, G. Bilger, M. Kaelin, F. J. Haug, H. Zogg, and A. N. Tiwari, "Effects of NaF Coevaporation on Structural Properties of Cu(In,Ga)Se_2 Thin Films," *Thin Solid Films* 431-432 (2003): 37–40.

44. R. Kaigawa, A. Morimotoa, K. Funahashia, et al., "Preparation of Wide Gap Cu(In,Ga)S_2 Films on ZnO Coated Substrates," *Thin Solid Films* 517 (2009): 2395–2398.

45. R. Kaigawa, T. Wada, S. Bakehe, and R. Klenk, "Three-Stage Evaporation of Cu(In,Ga)S_2 Solar Cell Absorber Films without KCN Treatment and Na Control," *Thin Solid Films* 511-512 (2006): 430–433.

46. M. Raghuwanshi, E. Cadel, S. Duguay, L. Arzel, N. Barreau, and P. Pareige, "Influence of Na on Grain Boundary and Properties of Cu(In,Ga)Se_2 Solar Cells," *Progress in Photovoltaics, Research and Applications* 25 (2017): 367–375.

47. S. Shukla, D. Adeleye, M. Sood, et al., "Carrier Recombination Mechanism and Photovoltage Deficit in 1.7-eV Band Gap Near-Stoichiometric Cu(In,Ga)S_2," *Physical Review Materials* 5 (2021): 055403.

48. S. Peedle, D. Adeleye, S. Shukla, S. Siebentritt, R. Oliver, and G. Kusch, "Role of Nanoscale Compositional Inhomogeneities in Limiting the Open Circuit Voltage in Cu(In,Ga)S_2 Solar Cells," *APL Energy* 1 (2023): 026104.

49. A. J.-C. M. Prot, M. Melchiorre, T. Schaaf, et al., "Improved Sequentially Processed Cu(In,Ga)(S,Se)$_2$ by Ag Alloying," *Solar RRL* 8 (2024): 2400208.

50. J. Mattheis, U. Rau, and J. H. Werner, "Light Absorption and Emission in Semiconductors With Band Gap Fluctuations—A Study on Cu(In,Ga)Se_2 Thin Films," *Journal of Applied Physics* 101 (2007): 113519.

51. W. Shockley and H. J. Queisser, "Detailed Balance Limit of Efficiency of P-N Junction Solar Cells," *Journal of Applied Physics* 32 (2004): 510–519.

52. M. Sood, D. Adeleye, S. Shukla, T. Torndahl, A. Hultqvist, and S. Siebentritt, "Low Temperature (Zn,Sn)O Deposition for Reducing Interface Open-Circuit Voltage Deficit to Achieve Highly Efficient Se-free Cu(In,Ga)S_2 Solar Cells," *Faraday Discussions* 239 (2022): 328–338.

53. Y. Hu, G. Kusch, D. Adeleye, S. Siebentritt, and R. Oliver, "Characterisation of the Interplay between Microstructure and Opto-Electronic Properties of Cu(In,Ga)S_2 Solar Cells by Using Correlative CL-EBSD Measurements," *Nanotechnology* 35 (2024): 295702.

54. S. Gharabeiki, F. Lodola, T. Schaaf, et al., "Effect of a Band-Gap Gradient on the Radiative Losses in the Open-Circuit Voltage of Solar Cells," *PRX Energy* 4 (2025): 033006.

55. A. J. C. M. Prot, M. Melchiorre, F. Dingwell, et al., "Composition Variations in Cu(In,Ga)(S,Se)$_2$ Solar Cells: Not a Gradient, but an Interlaced Network of Two Phases," *APL Materials* 11 (2023): 101120.

56. R. Scheer and H.-W. Schock, *Chalcogenide Photovoltaics: Physics, Technologies, and Thin Film Devices* (John Wiley & Sons, 2011).

57. D. Adeleye, M. Sood, A. V. Oli, et al., "Wide Gap Cu(In,Ga)S_2 Solar Cell: Mitigation of Phase Segregation in High Ga-content Thin Films Leads to Efficiencies Above 15.5%," *Small* 21 (2025): 2405221.

58. A. Redinger, S. Levcenko, C. J. Hages, D. Greiner, C. A. Kaufmann, and T. Unold, "Time Resolved Photoluminescence on cu (In, Ga)Se_2 Absorbers: Distinguishing Degradation and Trap States," *Applied Physics Letters* 110 (2017): 122104.

59. T. P. Weiss, B. Bissig, T. Feurer, R. Carron, S. Buecheler, and A. N. Tiwari, "Bulk and Surface Recombination Properties in Thin Film Semiconductors With Different Surface Treatments From Time-Resolved Photoluminescence Measurements," *Scientific Reports* 9 (2019): 5385.

60. A. Laemmle, R. Wuerz, and M. Powalla, "Efficiency Enhancement of Cu(In,Ga)Se_2 Thin-Film Solar Cells by a Post-Deposition Treatment With Potassium Fluoride," *physica status solidi (RRL) – Rapid Research Letters* 7 (2013): 631–634.

61. M. Sood, J. Bomasch, A. Lomuscio, et al., "Origin of Interface Limitation in Zn(O,S)/$CuInS_2$-Based Solar Cells," *ACS Applied Materials & Interfaces* 14 (2022): 9676–9684.

62. A. M. Gabor, J. R. Tuttle, D. S. Albin, M. A. Contreras, R. Noufi, and A. M. Hermann, "High-Efficiency $CuIn_xGa_{1-x}Se_2$ Solar Cells Made From $(In_x,Ga_{1-x})_2Se_3$ Precursor Films," *Applied Physics Letters* 65 (1994): 198–200.

63. P. de Francisco la, T. Ostasevicius, V. Tonaas Fauske, et al., *hyperspy/hyperspy: v2.1.1 (v2.1.1)* (Zenodo, 2024), https://doi.org/10.5281/zenodo.12724131.

64. J. F. O. J. Lähnemann, E. Prestat, H. W. Ånes, D. N. Johnstone, LGTM Migrator, and N. Tappy, *LumiSpy/Lumispy: v0.2.2 (v0.2.2)* (Zenodo, 2023), https://doi.org/10.5281/zenodo.7747350.

Supporting Information

Additional supporting information can be found online in the Supporting Information section. **Figure S1:** Deposition profile of CIGS with NaF co-evaporation. The bars in the schematic are the corresponding elemental fluxes, and the back thick line is the substrate temperature. The Mo-coated substrates were annealed in the beginning of the process without sulfur ambient to clean the surface. **Figure S2:** GGI and CGI ratios of CIGS measured at the (a) surface (7 kV) and (b) bulk (20 kV). (c) CGI profile of the absorbers measured from GDOES. Related to Figure 1. **Figure S3:** GDOES depth profiles of various elements in CIGS with different Na supplies during growth. Related to Figure 1. **Figure S4:** (a) Top view SEM image of 750°C NaF CIGS. Cross-sectional SEM images of CIGS absorbers with (b) 600°C and (c) 700°C NaF. Related to Figure 2a. **Figure S5:** (a) Wide-scan and (b) fine-scan X-ray diffractograms of CIGS with different Na supplies. (c) XRD patterns of CIGS (without NaF co-evaporation) before and after exfoliation from the Mo substrate. (d) Enlarged view of the dominant 112 reflex, showing a positive shift due to release of strain caused by the Mo substrate. The CIGS exfoliation process is described elsewhere [1, 2]. Related to Figure 2b. **Figure S6:** (a) One sun excited absolute PL spectra of CIGS with varying Na supplies and (b) the spectra in log scale to highlight low-intensity emissions. (c) PL spectra of 750 NaF absorber excited with 405 and 660 nm laser, both with 25 mW power. (d) Intensity-dependent PL spectra of LNG. CL spectra in (e) linear and (f) log scale. Related to Figure 3. **Figure S7:** Optoelectronic parameters derived from the PL and CL measurements. **Table S1:** Optoelectronic parameters derived from the PL and CL measurements. **Figure S8:** Cross-sectional mean CL spectrum for LNG, SLG, 650 NaF, and 750 NaF absorbers. Related to Figure 4. **Figure S9:** Line scans extracted from the NBE energy map shown in Figure 4c. The positions of line scan are as same as the positions in Figure S9. The extracted profiles highlight the graded bandgap feature of the absorber. For 650°C NaF, no energy change is observed after the notch, which extends to the surface. The large surface ratio for SLG and 750 NaF is due to artifacts from the empty area above the surface. Related to Figure 4. **Figure S10:** Cross sectional panchromatic CL map with line scan markers. The width of line scan is 2.5 µm. Related to Figure 5a. **Figure S11:** (a) Cross-sectional panchromatic CL map with narrow line scan markers. The width of line scan is 0.5 µm. (b) Corresponding CL line scan spectra across the depth. Related to Figure 5a. **Table S2:** TRPL fitted parameters. "A" represents the prefactors, and "**τ**" represents different lifetimes. Related to Figure 5b. **Figure S12:** Statistical distribution of the photovoltaic parameters of the solar cells. Related to Figure 6b. **Table S3:** Fitted dark *J–V* parameters for series resistance (R_s), shunt resistant (R_{sh}), diode factor (A), and dark current (J_0). Note that the buffer composition for LNG and SLG is different than 650 and 750 NaF. **Figure S13:** (a) EQE spectra of CIGS with varying Na supplies, alongside E_g extracted from the inflection point. Voltage-dependent EQE spectra of (b) SLG, (c) 650 NaF, and (d) 750 NaF absorber. Related to Figure 6c.